an elongated bipolar feature. The travel-time perturbations caused by the four events are all negative, with the maximum amplitude of 16.3 s. This is surprisingly strong. Recent theoretical studies, based on numerical simulations of emerging magnetic flux tubes, estimate the magnitude of travel-time anomalies at these depths to be of an order of 1 s (*23*). This discrepancy may imply that the magnetic field deep inside the convection zone is much stronger than in the models or that the magnetic field effects in the acoustic travel times are not yet well understood. However, the nature of the perturbations are not known, and the detected anomalies can be due to thermal rather than magnetic effects. In addition, a weak magnetic flux at large depths is probably undetectable by our method. Therefore, the disappearance of the travel-time anomalies after the start of emergence does not necessarily imply that sunspots are disconnected from their roots.

Our measurements and tests with several phase-speed filters also show that acoustic waves focused at depths of about 57 to 66 Mm have the biggest contribution to the signatures of emerging flux. The detection of such signatures at a depth of about 60 Mm possibly poses a low limit on the depth of generation of large magnetic regions. The average emergence speed from this depth up to the surface is estimated to be ~0.3 and 0.6 km/s for the analyzed weakest and strongest emerging flux events, respectively.

Predicting solar magnetic activity is a valuable tool for space weather forecasts. Our technique of imaging the deep solar interior, combined with uninterrupted helioseismic observations of the Solar Dynamics Observatory and the far-side imaging technique (*24*–*26*), can monitor the Sun's activity in a synoptic way, both in the near and the far sides, and allow detection of large sunspot regions before their appearance on the solar disc. Strong emerging flux events can now be anticipated 1 to 2 days in advance.

References and Notes

1. M. Ossendrijver, *Astron. Astrophys. Rev.* **11**, 287 (2003).
2. Y. Fan, *Sol. Phys.* **6**, 4 (2009).
3. B. C. Low, *J. Geophys. Res.* **106**, (A11), 25141 (2001).
4. S. K. Solanki, *Astron. Astrophys. Rev.* **11**, 153 (2003).
5. D. H. Hathaway, *Sol. Phys.* **7**, 1 (2010).
6. A. Brandenburg, *Astrophys. J.* **625**, 539 (2005).
7. V. V. Pipin, A. G. Kosovichev, *Astrophys. J.* **727**, L45 (2011).
8. T. L. Duvall Jr., S. M. Jefferies, J. W. Harvey, M. A. Pomerantz, *Nature* **362**, 430 (1993).
9. A. G. Kosovichev, T. L. Duvall Jr., P. H. Scherrer, *Sol. Phys.* **192**, 159 (2000).
10. H.-K. Chang, D.-Y. Chou, M.-T. Sun, *Astrophys. J.* **526**, L53 (1999).
11. J. M. Jensen, T. L. Duvall Jr., B. H. Jacobsen, J. Christensen-Dalsgaard, *Astrophys. J.* **553**, L193 (2001).
12. S. Zharkov, M. J. Thompson, *Sol. Phys.* **251**, 369 (2008).
13. A. G. Kosovichev, T. L. Duvall Jr., *ASP Conf. Ser.* **383**, 59 (2008).
14. A. G. Kosovichev, *Space Sci. Rev.* **144**, 175 (2009).
15. In the existing time-distance measurement scheme, an annulus is selected on the solar surface and cross-covariances are computed for diametrically opposite points of the annulus. All of the cross-covariances are then added together in order to increase the signal-to-noise ratio. Such a measurement scheme, widely known as a deep-focusing scheme (*27*), has all the selected acoustic ray paths focused on one point deep below the center of the annulus. Thus, the inferred travel-time variations essentially map local inhomogeneities around the focal point. By moving the center of the annulus to neighboring points of the observed area, it is possible to make a map of travel-time perturbations at a fixed depth.
16. In our approach, the oscillation signal is first averaged over an arc, and then cross-covariances are computed for every pair of diametrically opposite averaged arcs. This procedure has been already used, with an arc size of 90°, to determine the coefficients of absorption, emissivity reduction, and local suppression inside sunspots (*28*). In this configuration, every point in the annulus contributes to the oscillation signal of one and only one arc (fig. S1). Here, we select arcs of five different sizes—25.7°, 30°, 36°, 45°, and 60°—and average the corresponding cross-covariances in order to reduce the noise level. The position of the arcs along the annulus can be chosen arbitrarily. However, in order to eliminate anisotropic contributions in the computation of cross-covariances and further increase the signal-to-noise ratio, four different arc orientations are chosen for each of the five arc sizes. The orientations are determined so that starting from an arbitrary point, each one can be produced from the previous one by a fixed rotation, which depends on the arc size. If the arc size is N degrees, the rotation angle is $N/4$ degrees. In total, there are 20 configurations; each one is characterized by one of the five arc sizes and one of the four orientations for the given arc size.
17. We computed cross-covariances for every pair of diametrically opposite arcs using all of the 20 configurations described in (*16*) and repeated this procedure for 31 annuli, spanning a radius range of 55.5 to 99.0 Mm (Fig. 1). We then added all of the cross-covariances together and fitted the final cross-covariance with a Gabor wavelet (*29*) so as to determine the acoustic-phase travel time at a single pixel. If the same procedure is repeated for all pixels in the observed area, an acoustic travel-time map can be constructed. The signal-to-noise ratio of the travel-time map depends on the number of ray paths focused below the photosphere, and our results show that averaging over the 20 configurations and the 31 travel distances is sufficient to detect large emerging magnetic structures. It should also be noted that cross-covariances obtained from different travel distances have different phases and therefore can be added together only after appropriate travel-time shifts. We determined these travel-time shifts from the quiet-Sun measurements and made sure that no phase-shift cancellation occurs.
18. The data sets are 8-hour-long series of dopplergrams, tracked with a Carrington rotation rate and remapped into heliographic coordinates by using Postel's projection. The size of the tracked region is 256 by 256 pixels, with a spatial resolution of 0.12°/pixel. Each data set is filtered in the Fourier domain in order to extract the solar acoustic oscillation signals in the frequency range of 2 to 5 mHz, with phase speeds of 92 to 127 km/s. These waves have a 1-skip horizontal distance of 111 to 198 Mm, sampling the Sun's interior up to depths of 42 to 75 Mm (Fig. 1).
19. P. H. Scherrer *et al.*, *Sol. Phys.* **162**, 129 (1995).
20. We always refer to middle time of an 8-hour data set unless otherwise stated.
21. C. Lindsey, D. C. Braun, *Astrophys. J.* **620**, 1107 (2005).
22. J. Zhao, A. G. Kosovichev, *Astrophys. J.* **643**, 1317 (2006).
23. A. C. Birch, D. C. Braun, Y. Fan, *Astrophys. J.* **723**, L190 (2010).
24. C. Lindsey, D. C. Braun, *Science* **287**, 1799 (2000).
25. J. Zhao, *Astrophys. J.* **664**, L139 (2007).
26. S. Ilonidis, J. Zhao, T. Hartlep, *Sol. Phys.* **258**, 181 (2009).
27. T. L. Duvall Jr., in *Proc. GONG '94: Helio- and Astero-Seismology from the Earth and Space*, R. K. Ulrich, E. J. Rhodes Jr., W. Dappen, Eds. (ASPCS, San Francisco 1995), p. 76.
28. S. Ilonidis, J. Zhao, *Sol. Phys.* **268**, 377 (2011).
29. A. G. Kosovichev, T. L. Duvall, Jr., in *Proc. SCORe96 Workshop: Solar Convection and Oscillations and Their Relationship*, F.P. Pijpers, J. Christensen-Dalsgaard, C.S. Rosenthal, Eds. (Kluwer, Dordrecht, 1996), 241.

Acknowledgments: SOHO is a project of international cooperation between the European Space Agency and NASA. This work was partly supported by NASA contracts NNX09AI90G and NAS5-02139 to Stanford University and by Living With A Star–Targeted Research and Technology grant NNX07AP61. The data used in this work were obtained from http://soi.stanford.edu/data. The authors thank P. Scherrer and T. Duvall for reading the manuscript and providing useful comments. A.K. thanks the International Space Science Institute (Bern) for support.

Supporting Online Material

www.sciencemag.org/cgi/content/full/333/6045/993/DC1
Figs. S1 to S7

29 March 2011; accepted 14 July 2011
10.1126/science.1206253

Quantum Simulation of Frustrated Classical Magnetism in Triangular Optical Lattices

J. Struck,[1] C. Ölschläger,[1] R. Le Targat,[1] P. Soltan-Panahi,[1] A. Eckardt,[2] M. Lewenstein,[2,3] P. Windpassinger,[1] K. Sengstock[1]*

Magnetism plays a key role in modern technology and stimulates research in several branches of condensed matter physics. Although the theory of classical magnetism is well developed, the demonstration of a widely tunable experimental system has remained an elusive goal. Here, we present the realization of a large-scale simulator for classical magnetism on a triangular lattice by exploiting the particular properties of a quantum system. We use the motional degrees of freedom of atoms trapped in an optical lattice to simulate a large variety of magnetic phases: ferromagnetic, antiferromagnetic, and even frustrated spin configurations. A rich phase diagram is revealed with different types of phase transitions. Our results provide a route to study highly debated phases like spin-liquids as well as the dynamics of quantum phase transitions.

Frustrated spin systems belong to the most demanding problems of magnetism and condensed matter physics (*1*, *2*). The simplest realization of geometrical spin frustration is the triangular lattice (Fig. 1) with antiferromagnetic interactions: The spins cannot order in the favored antiparallel fashion and instead must compromise. The rich variety of possible spin

configurations in the quantum spin case arising from the competition between interactions and the geometry of the lattice has been studied in many different contexts (*3*, *4*). Classical frustrated spin systems also show intriguing properties (*5*–*7*), such as highly degenerate ground states, and emergent phenomena, such as artificial magnetic fields and monopoles observed in spin ice.

Despite the interest in magnetically frustrated systems, their experimental realization and characterization in "natural" solid-state devices still poses a major challenge. Recently, there have been considerable advances in the direction of simulating quantum magnetism (*8*–*15*). We report on a versatile simulator for large-scale classical magnetism on a two-dimensional (2D) triangular optical lattice (*16*) by exploiting the motional degrees of freedom of ultracold bosons (*17*). The cornerstone of our simulation is the independent tuning of the nearest-neighbor coupling elements J and J' (Fig. 1) by introducing a fast oscillation of the lattice (*18*). In particular, we can even control the sign of these elements (*19*, *20*), thus allowing for ferromagnetic or antiferromagnetic coupling schemes. Hence, we gain access to the whole diversity of expected complex magnetic phases in our 2D triangular system and can study large-system phase transitions as well as spontaneous symmetry-breaking caused by frustration. With our approach, the easily achievable Bose-Einstein condensate (BEC) temperatures are sufficient to observe Néel-ordered and spin-frustrated states. This is an advantage when compared with systems based on superexchange interaction (*10*), which demand much lower temperatures.

For weak interactions, ultracold bosonic atoms in an optical lattice form a superfluid state [in our 2D array of tubes: lattice depth is $5.6E_r$ (where E_r is the recoil energy of the lattice), on-site interaction $U = 0.004E_r$, single-particle tunneling $\tilde{J} = 0.002E_r$, and a maximum of 250 particles per tube]. In this case, the atoms at each site i of the lattice have a well-defined local phase θ_i that can, as a central concept here, be identified with a classical vector spin $\mathbf{S}_i = [\cos(\theta_i), \sin(\theta_i)]$ (see also Fig. 1). Long-range order of these local phases (spins) is imprinted by the minimization of the energy

$$E(\{\theta_i\}) = -\sum_{\langle i,j \rangle} J_{ij} \cos(\theta_i - \theta_j) = -\sum_{\langle i,j \rangle} J_{ij} \mathbf{S}_i \cdot \mathbf{S}_j \quad (1)$$

where the sum extends over all pairs of neighboring lattice sites. Note that we study large systems of ~1000 populated lattice sites. As a second central concept, the tunneling matrix elements J_{ij} assume the role of the "spin-spin" coupling parameters between neighboring lattice sites: Positive J_{ij} correspond to ferromagnetic interaction, and negative J_{ij} are consistent with antiferromagnetic interaction. The most important feature of our approach is the independent tuning of the tunneling parameters J and J' along two directions (Fig. 1) via an elliptical shaking of the lattice (*17*). This leads to various ferromagnetic, antiferromagnetic, and mixed-spin configurations (Fig. 2). In the situation where all tunneling parameters are positive (J, $J' > 0$), the spins align parallel, and we associate this with a fully ferromagnetically ordered phase. This is identical to the ordering observed without shaking. When, for example, the signs of the J' couplings are inverted ($J > 0$, $J' < 0$), the new ground state of the system is of rhombic order: Along the direction of negative coupling, the spins arrange in antiferromagnetic order, whereas the coupling in J direction remains ferromagnetic. The other configurations shown in Fig. 2 (spiral and chain order) can be explained in a similar fashion. Each of these spin configurations has its own, unique quasi-momentum distribution, which serves as a clear signature for identification via standard time-of-flight imaging techniques (*18*). The experimental data obtained for the different cases are presented in Fig. 2.

The rich variety of spin orders as a function of the control parameters J and J' can be mapped into the phase diagram (Fig. 3A). The background colors are meant to guide the eye and indicate the different spin configurations as expected from the minimization of the energy function (Eq. 1). We assign a symbol, representing the respective phase, to each data point by comparing the measured momentum distribution with the one obtained from theoretical calculations (*17*). The measured data matches very well with theory (*18*). The phase diagram has several interesting features that can be understood from the energy function (Eq. 1): First, the ferromagnetic phase (F) on the right-hand side ($J' > 0$) extends

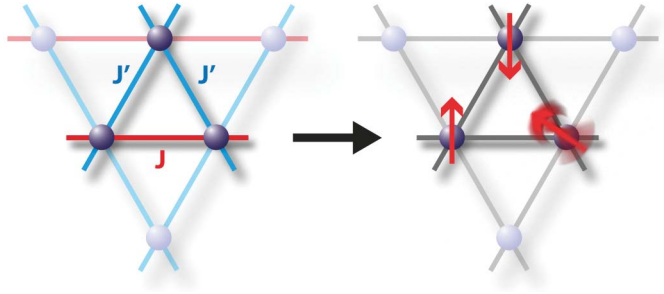

Fig. 1. Illustration of a single plaquette within a large-scale triangular lattice. The accessible, independent control parameters J and J' are highlighted. The local phase of the atoms residing on a single lattice site is mapped onto a classical vector spin (red arrows). The coupling parameters J and J' can be tuned ferro- or antiferromagnetically and determine the resulting spin configuration.

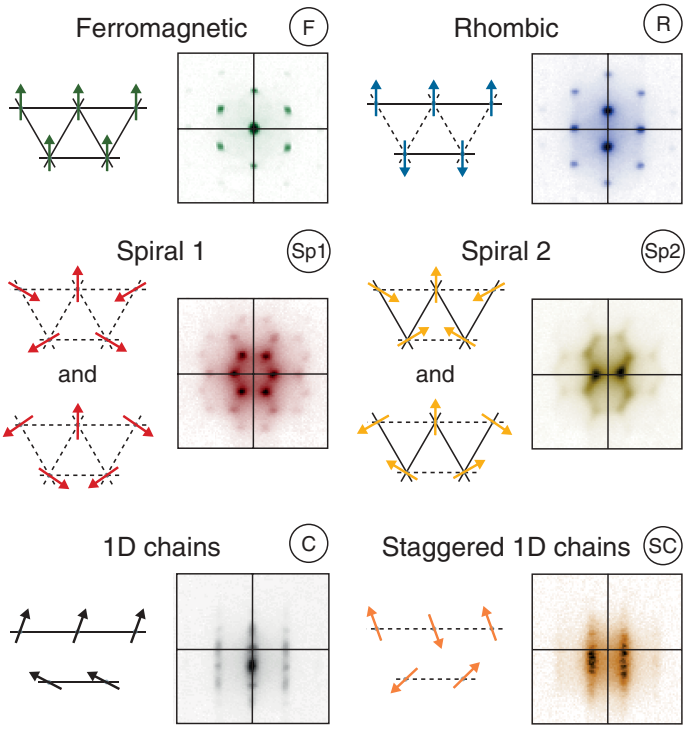

Fig. 2. Spin configurations in a triangular lattice and their experimental signatures. Sketches of small parts of the six relevant spin-orders, which can be realized within the large-scale lattice by tuning J and J', are shown. Solid and dashed lines indicate ferro- and antiferromagnetic couplings, respectively. In the spiral cases, two energetically degenerate spin configurations exist. The corresponding experimentally observed momentum distributions show distinct signatures. The axes in the experimental data mark the absolute position of the peaks. The pictures represent averages of several experimental runs. In the two spiral cases, because both ground-state configurations randomly appear, the signature of both modes is present in the average of consecutive pictures (see Fig. 4).

[1]Institut für Laserphysik, Universität Hamburg, D-22761 Hamburg, Germany. [2]Institut de Ciències Fotòniques, Mediterranean Technology Park, E-08860 Castelldefels, Barcelona, Spain. [3]Institució Catalana de Ricerca i Estudis Avançats, E-08010 Barcelona, Spain.

*To whom correspondence should be addressed. E-mail: klaus.sengstock@physnet.uni-hamburg.de

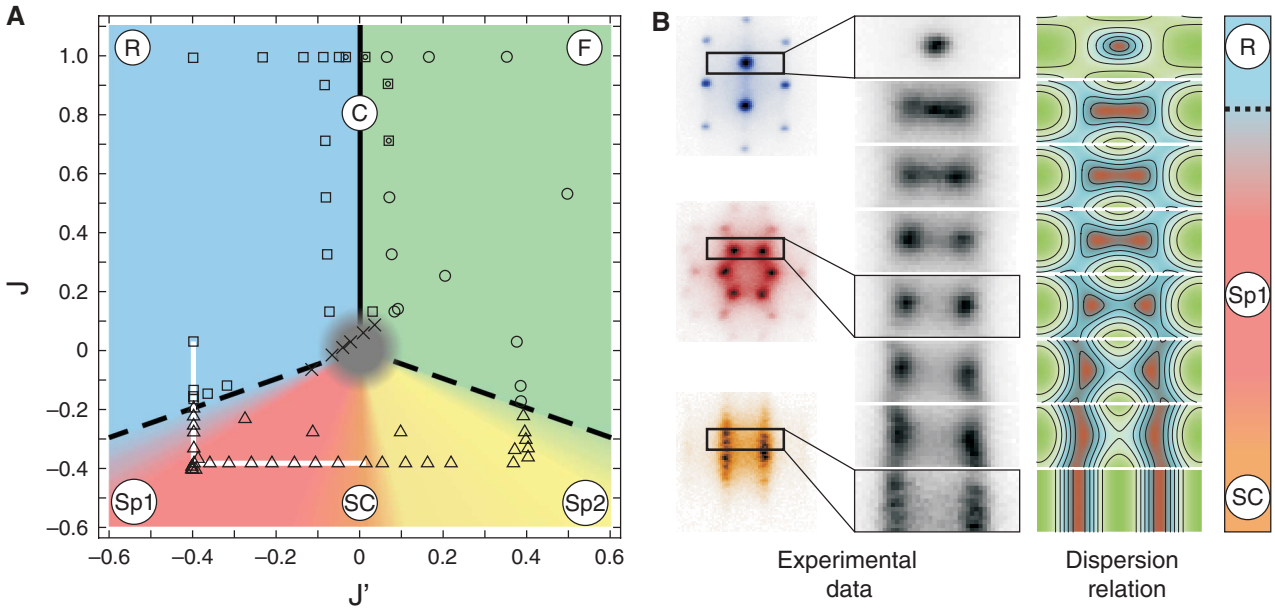

Fig. 3. Mapping of the magnetic phase diagram. (**A**) Phase diagram as a function of J and J', in units of the bare tunneling matrix elements. $J = J' = 1$ corresponds to no shaking. The solid line marks a first-order transition; dashed lines denote second-order transitions. Circles correspond to the experimental data for the ferromagnetic phase, squares to the rhombic phase, and triangles to the spiral phase. Crosses indicate data points with no long-range coherence. (**B**) Continuous change of the momentum structure in the spiral phase. (Left) Plot three examples of the whole momentum peak structure. The zoomed-in, uncolored data show the evolution of the peaks for measurements along the white line indicated in (A). (Right) For comparison, we also display the calculated lowest-band dispersion relation, which indicates where we theoretically expect the momentum peaks (highest density shown in red).

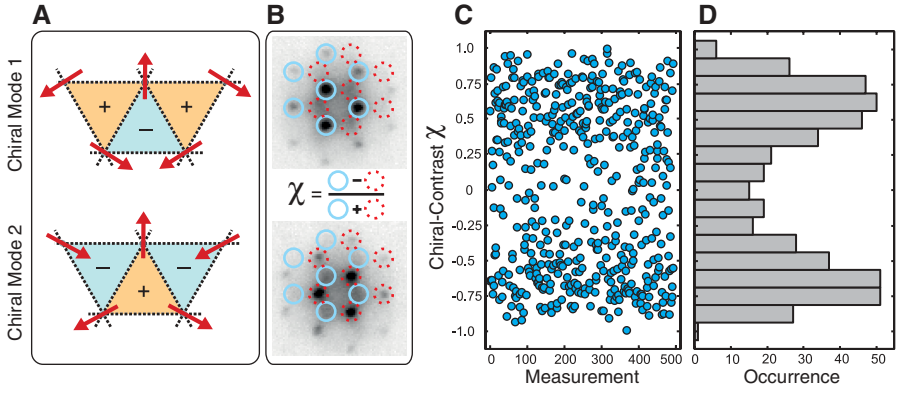

Fig. 4. Spontaneous symmetry-breaking in the Sp1 region for $J = J' = -0.4$. (**A**) Two different chiral configurations exist in the spiral case. The plus and minus signs indicate the value of the chiral order parameter. Red arrows denote vector spin. (**B**) The distinct momentum distributions of the modes allow for an unambiguous identification of the spin configurations. The chiral contrast χ is a measure for the occupancy of the two different orders. Positive values indicate a higher occupancy of the chiral mode 1; negative values signify the opposite. (**C**) Experimentally observed chiral contrast of ~500 consecutive measurements. The contrast is normalized to the highest absolute value of the series. (**D**) Corresponding histogram for the measurement series of (C) with a binning width of 0.125.

into regions where the J coupling already favors antiferromagnetic order. The same behavior is observed for the rhombic phase (R) ($J' < 0$), which extends to regions (J, $J' < 0$) with purely antiferromagnetic couplings. For $J < -|J'|/2$, frustration finally breaks the (anti)parallel spin order and leads to phases characterized by spiral spin configurations (Sp1, Sp2). In this region, the system possesses two energetically degenerate ground states, which we will discuss in more detail below. Second, the transitions between the phases are even of different nature. The transition from F to R is of first order. The experimental signature is a sudden change of the momentum distribution when crossing the phase boundary. In consequence, with limited experimental resolution, we see a collection of interference peaks belonging to both neighboring phases directly at the phase boundary in the averaged data of consecutive experimental runs (Fig. 2). The phase transitions into the spiral region (R to Sp1 and F to Sp2) are of second order. Finally, within the spiral region of the phase diagram, the spin configurations smoothly evolve. As a consequence, the staggered chain order found around $J' = 0$ is stable and experimentally well observable (Fig. 2). The gray shaded region in the center indicates that for small values of $|J|$ and $|J'|$ the long range spin order is lost, and the momentum distribution has no clear interference-peak structure.

We experimentally characterize the phase transition from R to Sp1 order as continuous (that is, second order) by following the evolution of the state when crossing the phase boundary (Fig. 3B). We observe a single momentum peak in the rhombic region of the phase diagram that smoothly splits into two once the trajectory enters the spiral region. This is in full agreement with the calculated dispersion relation also shown in the figure. The development of these two peaks marks the existence of two degenerate ground states. In this situation, the system is expected to randomly choose one of the possible states to thus exhibit spontaneous symmetry-breaking. We consider this important feature in more detail for the particular case of isotropic antiferromagnetic couplings ($J = J' < 0$). These two possible ground-state spin configurations (Fig. 4A) are mirror images of each other and can thus be distinguished by the chiral-order parameter (*18*) of upward- and downward-pointing plaquettes. Their different momentum distributions (Fig. 4B) allow for a direct distinction in the experiment. For consecutive experimental runs, each of the two spin configurations appears entirely random (Fig. 4C), which is clear evidence for the spontaneous nature of the symmetry-breaking

between the two ground states. In most cases (Fig. 4D), one of the modes clearly dominates. However, in some cases (below 10%), both configurations are almost equally populated at the same time. The simultaneous observation of two modes might be due to excitations like the formation of spin domains. Hence, for the first time, our system allows detailed studies on the mechanism of symmetry-breaking in large-scale "magnetic" systems.

A different aspect of our system is revealed when one recalls that the spin configurations actually correspond to local phases of a BEC at different sites of the triangular lattice. This provides new insight into unconventional superfluidity (*21*, *22*): For all phases except the ferromagnetic one, the state corresponds to a superfluid at nonzero quasi-momentum and, thus, nontrivial long-range phase order. Moreover, the observed spiral configurations spontaneously break time-reversal symmetry by showing circular bosonic currents around the triangular plaquettes of the lattice. Clockwise and counterclockwise currents are found in a staggered fashion from plaquette to plaquette. These resemble the currents of the staggered flux state thought to play a role in explaining the pseudogap phase of high-temperature cuprate superconductors (*23*).

Our results demonstrate the realization of a simulator for classical magnetism in a triangular lattice. Let us point out here that these results are obtained simply by using spinless bosons. Due to the high degree of controllability, we succeeded in observing all of the various magnetic phases and phase transitions of first and second order, as well as frustration-induced spontaneous symmetry-breaking. It now becomes possible to quench systems on variable time scales from ferromagnetic to antiferromagnetic couplings and to study the complex relaxation dynamics. Furthermore, extending the studies to the strongly correlated regime promises to give a deeper insight into the understanding of quantum spin models and spin-liquid–like phases (*24*).

References and Notes

1. L. Pauling, *J. Am. Chem. Soc.* **57**, 2680 (1935).
2. G. H. Wannier, *Phys. Rev.* **79**, 357 (1950).
3. L. Balents, *Nature* **464**, 199 (2010).
4. S. Sachdev, *Nat. Phys.* **4**, 173 (2008).
5. R. Moessner, A. P. Ramirez, *Phys. Today* **59**, 24 (2006).
6. D. J. P. Morris *et al.*, *Science* **326**, 411 (2009); 10.1126/science.1178868.
7. T. Fennell *et al.*, *Science* **326**, 415 (2009); 10.1126/science.1177582.
8. M. Lewenstein *et al.*, *Adv. Phys.* **56**, 243 (2007).
9. I. Bloch, J. Dalibard, W. Zwerger, *Rev. Mod. Phys.* **80**, 885 (2008).
10. S. Trotzky *et al.*, *Science* **319**, 295 (2008); 10.1126/science.1150841.
11. K. Kim *et al.*, *Nature* **465**, 590 (2010).
12. X.-S. Ma, B. Dakic, W. Naylor, A. Zeilinger, P. Walther, *Nat. Phys.* **7**, 399 (2011).
13. Y.-J. Lin, R. L. Compton, K. Jiménez-García, J. V. Porto, I. B. Spielman, *Nature* **462**, 628 (2009).
14. W. Zwerger, *Science* **325**, 1507 (2009).
15. J. Simon *et al.*, *Nature* **472**, 307 (2011).
16. C. Becker *et al.*, *N. J. Phys.* **12**, 065025 (2010).
17. A. Eckardt *et al.*, *Europhys. Lett.* **89**, 10010 (2010).
18. Supporting material is available on *Science* Online.
19. A. Eckardt, C. Weiss, M. Holthaus, *Phys. Rev. Lett.* **95**, 260404 (2005).
20. H. Lignier *et al.*, *Phys. Rev. Lett.* **99**, 220403 (2007).
21. G. Wirth, M. Ölschläger, A. Hemmerich, *Nat. Phys.* **7**, 147 (2011).
22. P. Soltan-Panahi, D.-S. Lühmann, J. Struck, P. Windpassinger, K. Sengstock, http://arXiv.org/abs/1104.3456.
23. P. A. Lee, N. Nagaosa, X.-G. Wen, *Rev. Mod. Phys.* **78**, 17 (2006).
24. R. Schmied, T. Roscilde, V. Murg, D. Porras, J. I. Cirac, *N. J. Phys.* **10**, 045017 (2008).

Acknowledgments: We thank A. Rosch, P. Hauke, and D.-S. Lühmann for stimulating discussions and the Deutsche Forschungsgemeinschaft (FOR 801, GRK 1355) and the Landesexzellenzinitiative Hamburg, which is supported by the Joachim Herz Stiftung, for funding. A.E. and M.L. are grateful for support through the Spanish Ministerio de Ciencia y Innovación grant TOQATA, European Research Council grant QUAGATUA, and European Union grants AQUTE and NAMEQUAM.

Supporting Online Material

www.sciencemag.org/cgi/content/full/science.1207239/DC1
SOM Text
Figs. S1 and S2
References

19 April 2011; accepted 8 July 2011
Published online 21 July 2011;
10.1126/science.1207239

Visualizing Individual Nitrogen Dopants in Monolayer Graphene

Liuyan Zhao,[1] Rui He,[1] Kwang Taeg Rim,[2] Theanne Schiros,[3] Keun Soo Kim,[1,4] Hui Zhou,[1] Christopher Gutiérrez,[1] S. P. Chockalingam,[1] Carlos J. Arguello,[1] Lucia Pálová,[2] Dennis Nordlund,[5] Mark S. Hybertsen,[6] David R. Reichman,[2] Tony F. Heinz,[1,7] Philip Kim,[1] Aron Pinczuk,[1,8] George W. Flynn,[2] Abhay N. Pasupathy[1]*

In monolayer graphene, substitutional doping during growth can be used to alter its electronic properties. We used scanning tunneling microscopy, Raman spectroscopy, x-ray spectroscopy, and first principles calculations to characterize individual nitrogen dopants in monolayer graphene grown on a copper substrate. Individual nitrogen atoms were incorporated as graphitic dopants, and a fraction of the extra electron on each nitrogen atom was delocalized into the graphene lattice. The electronic structure of nitrogen-doped graphene was strongly modified only within a few lattice spacings of the site of the nitrogen dopant. These findings show that chemical doping is a promising route to achieving high-quality graphene films with a large carrier concentration.

Substitutional doping is a powerful way to tailor material properties at the nanoscale (*1*), and it might be expected to have fundamentally different consequences when used to alter the electronic properties of inherently two-dimensional (2D) materials such as graphene (*2*). In recent years, several experimental techniques have been developed to dope the carbon lattice (*3*–*9*). These include methods applied during growth of large-area graphene films (*4*, *5*, *7*, *8*) and ways to modify the material after growth (*3*, *6*), as well as a new one-pot procedure to produce highly doped, few-layer graphitic structures (*9*). Several characterization techniques including x-ray photoemission (*10*, *11*), Raman spectroscopy (*3*, *5*, *7*) and transmission electron microscopy (*12*) have been used to analyze the effect of the doping process in graphene. However, a microscopic understanding of the atomic and low-energy electronic structure induced by the substitutional doping process in monolayer graphene is lacking. In our experiment, we used the atomic-resolution imaging capabilities of the scanning tunneling microscope to understand the local structure in the vicinity of a N dopant in monolayer graphene and spectroscopic imaging to measure the density of states and carrier concentration at the nanoscale. We also report scanning Raman spectroscopy, core-level x-ray spectroscopy and first principles calculations to characterize the effect of N-doping on the graphene film.

We grew N-doped graphene films using chemical vapor deposition on copper foil substrates (*13*) in a quartz tube furnace [sample growth details in supporting online material (SOM) I (a)]. Each graphene-covered foil was divided into three parts and immediately studied using Raman spectroscopy, x-ray spectroscopy, and scanning tunneling microscopy (STM) measurements. Samples have been characterized as grown on copper foils as well as after transfer to an insulating SiO_2 substrate [sample transfer and preparation details in SOM I, (b) to (d)].

Raman spectra (Fig. 1A) were taken over large areas (20-μm spot size) of the N-doped

[1]Department of Physics, Columbia University, New York, NY 10027, USA. [2]Department of Chemistry, Columbia University, New York, NY 10027, USA. [3]Energy Frontier Research Center, Columbia University, New York, NY 10027, USA. [4]Department of Physics and Graphene Research Institute, Sejong University, Seoul 143-747, Korea. [5]Stanford Synchrotron Radiation Lightsource, SLAC National Accelerator Laboratory, Menlo Park, CA 94025, USA. [6]Center for Functional Nanomaterials, Brookhaven National Laboratory, Upton, NY 11973–5000, USA. [7]Department of Electrical Engineering, Columbia University, New York, NY 10027, USA. [8]Department of Applied Physics and Applied Mathematics, Columbia University, New York, NY 10027, USA.

*To whom correspondence should be addressed. E-mail: pasupathy@phys.columbia.edu